SIAM J. SCI. STAT. COMPUT.
Vol. 13, No. 5, pp. 1097–1122, September 1992

004



# A COMPARISON OF THREE MIXED METHODS FOR THE TIME-DEPENDENT MAXWELL'S EQUATIONS*

PETER MONK†

**Abstract.** Three mixed finite-element methods for approximating Maxwell's equations are compared. A dispersion analysis provides a Courant–Friedrichs–Lewy (CFL) bound that is necessary for convergence when a uniform mesh is used. The dispersion analysis also allows a comparison of the stability properties of the methods. Superconvergence at the interpolation points is proved for uniform grids, and demonstrated by three numerical examples. All three methods are shown to be able to handle discontinuous media without modification of the finite-element spaces. Since all three methods have three-dimensional counterparts, this study suggests that all three methods could be the basis of a successful three-dimensional code.

**Key words.** Maxwell's equations, finite elements, mixed methods

**AMS(MOS) subject classifications.** 65N30, 78-08

## 1. Introduction.

In a recent paper, Lee and Madsen [9] present numerical results for a novel mixed finite-element method for approximating the time-dependent Maxwell's equations. Applying the method to two-dimensional problems, they show, by numerical examples, that their method has good dispersion properties and can handle discontinuous dielectric constants without special modification of the finite-element spaces. The purpose of this paper is to investigate the dispersion properties of the Lee–Madsen method analytically, and to compare the algorithm to two other mixed finite-element methods due (in three dimensions) to Nédélec [13] and Monk [12]. The Nédélec scheme is of particular interest since it uses a special space of piecewise linear polynomials to approximate the electric field, yet does not need modification where the dielectric constant is discontinuous. This is in contrast to methods based on standard continuous piecewise linear elements (cf. [9]). Our analysis will also show the connection between the mixed finite-element methods analyzed in this paper and the standard Yee finite-difference method for Maxwell's equations [18].

Our study is limited to Maxwell's equations in two space dimensions. Of course this is not the setting of real physical interest; however, the two-dimensional case makes a convenient test problem for rapid comparison of methods. Unfortunately, some features of Maxwell's equations, such as the divergence-free nature of the magnetic flux density, are lost in the two-dimensional case.

Besides the paper of Lee and Madsen [9], Adam, Serveniere, Nédélec, and Raviart [1] have also examined the use of mixed methods to discretize Maxwell's equations. The method of Adam et al. [1] is closely related to the two-dimensional analogue of the method of Monk [12], but does not allow for discontinuous dielectric constant or conductivity. Adam et al. [1] present a dispersion and error analysis for their method in the case when the mass matrix is lumped. In this paper we deal with the full mass matrix and allow discontinuous coefficients.

The method of Lee and Madsen is also related to a prior method suggested by Cangellaris, Lin, and Mei [3]. They proposed and discussed a point-matching (or collocation) method based on the use of continuous bilinear finite-element spaces for

* Received by the editors September 24, 1990; accepted for publication (in revised form) June 28, 1991. This research was supported in part by grants from the Air Force Office of Scientific Research and the National Science Foundation.

† Department of Mathematical Sciences, University of Delaware, Newark, Delaware 19716 (monk@math.udel.edu).

both the electric and magnetic fields, but on staggered grids. For other references concerning the use of finite-element methods in discretizing Maxwell's equations, see [9], and for a discussion of developments in finite-difference methods, see [16].

The plan of the paper is as follows. In §2 we discuss two general classes of variational principles for the time-dependent Maxwell system. Then in §3 we give details of the three finite-element methods examined in this paper. We discuss error estimates and derive the discrete equations in the special case of a uniform grid. These equations show the connections between the methods in this paper and standard finite-difference methods (cf. [18]). In §4, we use the discrete equations on a uniform grid to compare the three methods via a dispersion analysis. Section 5 is devoted to numerical experiments with the three methods. For ease of comparison, we have used examples from [9] as test problems.

**2. Variational principles for Maxwell's equations.** We begin by deriving two general classes of methods for Maxwell's equations [9], [13], [12], [11]. Since our numerical examples are all in two space dimensions, we consider Maxwell's equations for a linear isotropic material in which the magnetic field $\boldsymbol{H}$ is $z$-polarized. Thus if $\boldsymbol{E} = (E^{(1)}(\boldsymbol{x},t), E^{(2)}(\boldsymbol{x},t))$ and $\boldsymbol{H} = H(\boldsymbol{x},t)$ where $\boldsymbol{x} = (x,y)$, we have that

$$\epsilon \frac{\partial \boldsymbol{E}}{\partial t} + \sigma \boldsymbol{E} = \vec{\nabla} \times H - \boldsymbol{J}, \tag{1}$$

$$\mu \frac{\partial H}{\partial t} = -\nabla \times \boldsymbol{E}, \tag{2}$$

where $\epsilon, \sigma$, and $\mu$ are known functions of $\boldsymbol{x}$ giving the dielectric constant ($\epsilon$), permeability ($\mu$), and conductivity ($\sigma$), respectively. $\boldsymbol{J} = (J^{(1)}, J^{(2)})$ is a function of space and time giving the current density. The vector curl ($\vec{\nabla}\times$) is defined by

$$\vec{\nabla} \times f = \left( \frac{\partial f}{\partial y}, -\frac{\partial f}{\partial x} \right), \tag{3}$$

and the scalar curl ($\nabla\times$) by

$$\nabla \times \boldsymbol{v} = \frac{\partial}{\partial x} v^{(2)} - \frac{\partial}{\partial y} v^{(1)} \tag{4}$$

(we use $v^{(j)}$ to refer to the $j$th component of a vector $\boldsymbol{v}$). Equations (1) and (2) are solved in a plane polygonal region $\Omega$ with boundary $\Gamma$ and we assume the boundary condition

$$\boldsymbol{n} \times \boldsymbol{E} = \gamma, \tag{5}$$

where $\boldsymbol{n}$ is the unit outward normal to $\Omega$, $\boldsymbol{n} \times \boldsymbol{E} = E^{(1)} n^{(2)} - E^{(2)} n^{(1)}$ and $\gamma$ is a specified function. If $\gamma \equiv 0$, this boundary condition models a perfect conducting boundary. In addition, initial data must be specified so that we assume that

$$\boldsymbol{E}(0) = \boldsymbol{E}_0 \quad \text{and} \quad H(0) = H_0, \tag{6}$$

where $\boldsymbol{E}_0$ and $H_0$ are given functions. Equations (1), (2), (5), and (6) are a well-posed system of equations (cf. [5], [1], [10]) provided $\epsilon, \mu, \gamma, \sigma$, and $\boldsymbol{J}$ are sufficiently smooth and satisfy standard positivity and boundedness assumptions.

To derive a weak or variational formulation of (1)–(6), we proceed formally (for details of the function space setting, see [5], [12]). Multiplying (1) by a test function

$\boldsymbol{\phi}(\boldsymbol{x})$ and (2) by $\psi(\boldsymbol{x})$ and integrating over $\Omega$, we obtain the following equations where $(\boldsymbol{u},\boldsymbol{v}) = \int_\Omega u^{(1)}v^{(1)} + u^{(2)}v^{(2)}\,dA$ and $(u,v) = \int_\Omega uv\,dA$,

$$(\epsilon \boldsymbol{E}_t + \sigma \boldsymbol{E}, \boldsymbol{\phi}) = (\vec{\nabla} \times H, \boldsymbol{\phi}) - (\boldsymbol{J}, \boldsymbol{\phi}), \tag{7}$$

$$(\mu, H_t, \psi) = -(\nabla \times \boldsymbol{E}, \psi). \tag{8}$$

This pair of equations is not suitable for discretization since, in general, it would not result in an energy-conserving discrete problem. Instead we choose to integrate one of the curl terms in (7) or (8) by parts. One choice will lead to the method of Lee and Madsen, the other to the method of Nédélec.

Let

$$H(\mathrm{curl};\Omega) = \{\boldsymbol{u} \in (L^2(\Omega))^2 \mid \nabla \times \boldsymbol{u} \in L^2(\Omega)\},$$
$$H_0(\mathrm{curl};\Omega) = \{\boldsymbol{u} \in H(\mathrm{curl};\Omega) \mid \boldsymbol{n} \times \boldsymbol{u} = 0 \text{ on } \Gamma\},$$

and let $\boldsymbol{E}(t) = \boldsymbol{E}(\cdot,t)$ and $H(t) = H(\cdot,t)$ (see [6] for a complete discussion of the curl spaces). If we integrate (7) by parts, then provided $\boldsymbol{\phi} \in H_0(\mathrm{curl};\Omega)$ we are led to the conclusion that $\boldsymbol{E}(t) \in H(\mathrm{curl};\Omega), H(t) \in L^2(\Omega)$ satisfies

$$(\epsilon \boldsymbol{E}_t + \sigma \boldsymbol{E}, \boldsymbol{\phi}) = (H, \nabla \times \boldsymbol{\phi}) - (\boldsymbol{J}, \boldsymbol{\phi}) \quad \forall \boldsymbol{\phi} \in H_0(\mathrm{curl};\Omega), \tag{9}$$

$$(\mu H_t, \psi) = -(\nabla \times \boldsymbol{E}, \psi) \quad \forall \psi \in L^2(\Omega), \tag{10}$$

and

$$\boldsymbol{n} \times \boldsymbol{E} = \gamma \quad \text{on } \Gamma, \tag{11}$$

together with the initial condition (6). Note that in this case the test function $\boldsymbol{\phi}$ must have a well-defined scalar curl and must satisfy the boundary condition $\boldsymbol{n} \times \boldsymbol{\phi} = 0$. In this formulation the boundary conditions are essential. Nédélec's method is based on (9)–(11).

Alternatively, we may integrate (8) by parts to obtain that $\boldsymbol{E}(t) \in (L^2(\Omega))^2$ and $H(t) \in H(\vec{\mathrm{curl}};\Omega) \equiv \{v \in L^2(\Omega) | \vec{\nabla} \times v \in (L^2(\Omega))^2\}$ satisfy

$$(\epsilon \boldsymbol{E}_t + \sigma \boldsymbol{E}, \boldsymbol{\phi}) = (\vec{\nabla} \times H, \boldsymbol{\phi}) - (\boldsymbol{J}, \boldsymbol{\phi}) \quad \forall \boldsymbol{\phi} \in (L^2(\Omega))^2, \tag{12}$$

$$(\mu H_t, \psi) = -(\boldsymbol{E}, \vec{\nabla} \times \psi) + \langle \gamma, \psi \rangle \quad \forall \psi \in H(\vec{\mathrm{curl}};\Omega), \tag{13}$$

together with the initial condition (6). Note that in this case neither trial nor test functions need to satisfy any boundary conditions, and the boundary condition $\boldsymbol{n} \times \boldsymbol{E} = \gamma$ is imposed naturally. The system (12)–(13) is the basis for the method of Lee–Madsen [9] and the method of Monk [12].

Next we discretize in space to produce an approximate method of lines for Maxwell's equations. Later we shall detail discretization in time. To discretize (9)–(11) we let $U_h^N \subset H(\mathrm{curl};\Omega), U_{ho}^N = U_h^N \cap H_0(\mathrm{curl};\Omega)$, and $V_h^N \subset L^2(\Omega)$ be finite-dimensional spaces indexed by $h$. In this paper each space will be a finite-element space, but at this stage we could allow other possibilities, such as spectral method spaces. The semidiscrete problem corresponding to (9)–(11) is to find $(\boldsymbol{E}^h(t), H^h(t)) \in U_h^N \times V_h^N$ such that

$$(\epsilon \boldsymbol{E}_t^h + \sigma \boldsymbol{E}^h, \boldsymbol{\phi}^h) = (H^h, \nabla \times \boldsymbol{\phi}^h) - (\boldsymbol{J}, \boldsymbol{\phi}^h) \quad \forall \boldsymbol{\phi}^h \in U_{ho}^N, \tag{14}$$

$$(\mu H_t^h, \psi^h) = -(\nabla \times \boldsymbol{E}^h, \psi^h) \quad \forall \psi^h \in V_h^N, \tag{15}$$

$$\boldsymbol{n} \times \boldsymbol{E}^h = \gamma^h \quad \text{on } \Gamma, \tag{16}$$

and

$$\boldsymbol{E}^h(0) = \boldsymbol{E}_0^h \quad \text{and} \quad H^h(0) = H_0^h, \tag{17}$$

where $\gamma^h \in \boldsymbol{n} \times U_h^N$ approximates $\gamma$, $\boldsymbol{E}_0^h \subset U_h^N$ approximates $\boldsymbol{E}_0$, and $H_0^h \subset V_h^N$ approximates $H_0$. Note that $U_h^N$ need only be a subspace of $H(\mathrm{curl};\Omega)$ and need not be in $(H^1(\Omega))^2$. Standard continuous linear finite elements are in $(H^1(\Omega))^2$ and thus are too smooth. This manifests itself in the complex way that standard elements must be adapted to handle interfaces where $\epsilon$ is discontinuous (cf. [9] and §5.3 of this paper). Nédélec's construction gives elements in $H(\mathrm{curl};\Omega)$ but not in $(H^1(\Omega))^2$.

To discretize (12)–(13) we take finite-dimensional spaces $U_h^L \subset (L^2(\Omega))^2$ and $V_h^L \subset H(\vec{\mathrm{curl}};\Omega)$. Then seek $(\boldsymbol{E}^h(t), H^h(t)) \in U_h^L \times V_h^L$ such that

$$(\epsilon \boldsymbol{E}_t^h + \sigma \boldsymbol{E}^h, \boldsymbol{\phi}^h) = (\vec{\nabla} \times H^h, \boldsymbol{\phi}^h) - (J, \boldsymbol{\phi}^h) \quad \forall \boldsymbol{\phi} \in U_h^L, \tag{18}$$

$$(\mu H_t^h, \psi^h) = -(\boldsymbol{E}^h, \vec{\nabla} \times \psi^h) + \langle \gamma, \psi^h \rangle \quad \forall \psi^h \in V_h^L, \tag{19}$$

and

$$\boldsymbol{E}^h(0) = E_0^h \quad \text{and} \quad H^h(0) = H_0^h, \tag{20}$$

where $\boldsymbol{E}_0^h \subset U_h^L$ and $H_0^h \subset V_h^L$, respectively, approximate $\boldsymbol{E}_0$ and $H_0$.

In this case, the boundary condition need not be imposed on the finite-element functions. Note that $V_h^L \subset H(\vec{\mathrm{curl}};\Omega)$ and so, in this two-dimensional problem, we need $V_h^L \subset H^1(\Omega)$. Thus in this case, standard finite elements can be used to construct $V_h^L$. In fact, Lee and Madsen [9] use standard isoparametric piecewise bilinear functions on quadrilateral elements. The space $U_h^L \subset (L^2(\Omega))^2$, and thus a candidate space, is the space of piecewise constant vectors, which is the choice used by Lee and Madsen [9]. Monk [12] uses a slightly augmented space.

One final remark is that the general methods (14)–(17) and (18)–(20) both conserve energy (before time discretization). To see this, consider the case when $\sigma \equiv 0$, $\boldsymbol{J} \equiv 0$, $\gamma \equiv 0$. Then taking $\psi^h = H^h$ and $\boldsymbol{\phi}^h = \boldsymbol{E}^h$ in (14)–(17) or (18)–(19) and adding (14)–(15) or (18)–(19) we obtain

$$(\epsilon \boldsymbol{E}_t^h, \boldsymbol{E}^h) + (\mu H_t^h, H^h) = 0. \tag{21}$$

Thus

$$\frac{1}{2}\frac{d}{dt}\{(\epsilon \boldsymbol{E}^h, \boldsymbol{E}^h) + (\mu H^h, H^h)\} = 0,$$

and so,

$$(\epsilon \boldsymbol{E}^h(t), \boldsymbol{E}^h(t)) + (\mu H^h(t), H^h(t)) = (\epsilon \boldsymbol{E}^h(0), \boldsymbol{E}^h(0)) + (\mu H^h(0), H^h(0)), \tag{22}$$

which states that the energy in the discrete system is independent of time. This energy conservation is the reason for integrating by parts in (7) and (8) to ensure that the curl terms cancel. The above energy equality can be used to derive error estimates for the finite-element methods (see [11] and §3 of this paper).

**3. Discretization in space and time.** In this section we give details of each of the methods to be analyzed. We start by subdividing $\Omega$ using a collection of quadrilateral elements $\tau_h = \{K_i\}_{i=1}^{N_h}$ with maximum diameter $h$, which obey the usual finite-element mesh restrictions [4]. The basis functions for each finite-element

space are obtained using the isoparametric method by mapping basis functions on a reference element to the target element. Let the domain of the reference element be

$$\hat{K} = \{(x, y) \mid 0 \le \hat{x} \le 1,\ 0 \le \hat{y} \le 1\}, \tag{23}$$

then let $\boldsymbol{F}_{K_i}$ be the bilinear map from $\hat{K}$ to $K_i$. If $K_i$ has vertices with coordinates $\{\boldsymbol{a}_j^{(i)}\}_{j=1}^4$ and $\hat{\boldsymbol{x}} = (\hat{x}, \hat{y})$, then

$$\boldsymbol{F}_{K_i}(\hat{\boldsymbol{x}}) = \boldsymbol{a}_1^{(i)}(1-\hat{x})(1-\hat{y}) + \boldsymbol{a}_2^{(i)}\hat{x}(1-\hat{y}) + \boldsymbol{a}_3^{(i)}\hat{x}\hat{y} + \boldsymbol{a}_4^{(i)}(1-\hat{x})\hat{y}. \tag{24}$$

We denote the Jacobian of $\boldsymbol{F}_{K_i}$ by $\boldsymbol{J}_{K_i}(\hat{x})$.

In general,

$$\boldsymbol{E}^h(t) = \sum_{j=1}^{N_E} E_j(t)\boldsymbol{\phi}_j(\boldsymbol{x}) \quad \text{and} \quad H^h(t) = \sum_{j=1}^{N_H} H_j\psi_j(\boldsymbol{x}), \tag{25}$$

where $N_E$ and $N_H$ are the number of degrees of freedom for $\boldsymbol{E}^h$ and $H^h$, respectively, and $\{\boldsymbol{\phi}_j(\boldsymbol{x})\}_{j=1}^{N_E}$ and $\{\psi_j(x)\}_{j=1}^{N_H}$ are suitable basis functions.

In the remainder of the paper we use the notation that $Q_{ij}$ is the set of all polynomials of degree at most $i$ in $x$ and at most $j$ in $y$. Thus $Q_{00}$ is the space of constant functions and $Q_{10} = \{p \mid p = a + bx \quad a, b \in \mathbb{R}\}$.

**3.1. Lee and Madsen's method.** This method has the simplest spaces. The electric field space is just the space of piecewise constant vectors. Thus

$$U_h^L = \{\boldsymbol{u}^h \mid \boldsymbol{u}^h|_K \in Q_{00} \times Q_{00} \quad \forall K \in \tau_h\}. \tag{26}$$

A suitable basis for this space is the set of piecewise constant vector functions in which one component is nonzero on exactly one element in the grid. The space $V_h^L$ is the standard continuous piecewise bilinear isoparametric space. Thus to construct $V_h^L$, we define the reference element $(\hat{K}, P_{\hat{K}}, \Sigma_{\hat{K}})$ [4] by taking $\hat{K}$ to be the reference domain in (23) with vertices $\{\hat{\boldsymbol{a}}_i\}_{i=1}^4$, the local space $P_{\hat{K}}$ to be the standard space of bilinear polynomials so that $P_{\hat{K}} = Q_{11}$, and the local degrees of freedom to be

$$\Sigma_{\hat{K}} = \{p(\hat{\boldsymbol{a}}_i) \mid 1 \le i \le 4\}. \tag{27}$$

Then on each element $K \in \tau_h$ we have that the $j$th basis function is given by $\psi_j|_K(\boldsymbol{x}) = \hat{\psi}(F_K^{-1}(\boldsymbol{x}))$ for some $\hat{\psi} \in P_{\hat{K}}$. Thus

$$V_h^L = \{v_h \in C(\overline{\Omega}) \mid v_h|_K = \hat{v}_K \circ F_K^{-1} \quad \text{for some} \quad \hat{v}_K \in Q_{11} \quad \forall K \in \tau_h\}. \tag{28}$$

Following the isoparametric philosophy, all integrations are performed on $\hat{K}$ by mapping from a given element $K$ to $\hat{K}$ using the mapping $F_K^{-1}$. We use four-point Gaussian quadrature on $\hat{K}$ to compute integrals. This is exact if $F_K$ is affine and of precision three in general.

In summary, the degrees of freedom for the discontinuous electric field space $U_h^L$ are the values of the electric field at the centroid of each element. The degrees of freedom for the magnetic field space $V_h^L$ are the values of the field at the vertices of the mesh. In keeping with Lee and Madson [9], we refer to this method as ECHL ($E$ constant, $H$ linear).

We now apply the ECHL algorithm on a uniform mesh and consider the equations satisfied by the degrees of freedom. Figure 1 shows a portion of the mesh for the

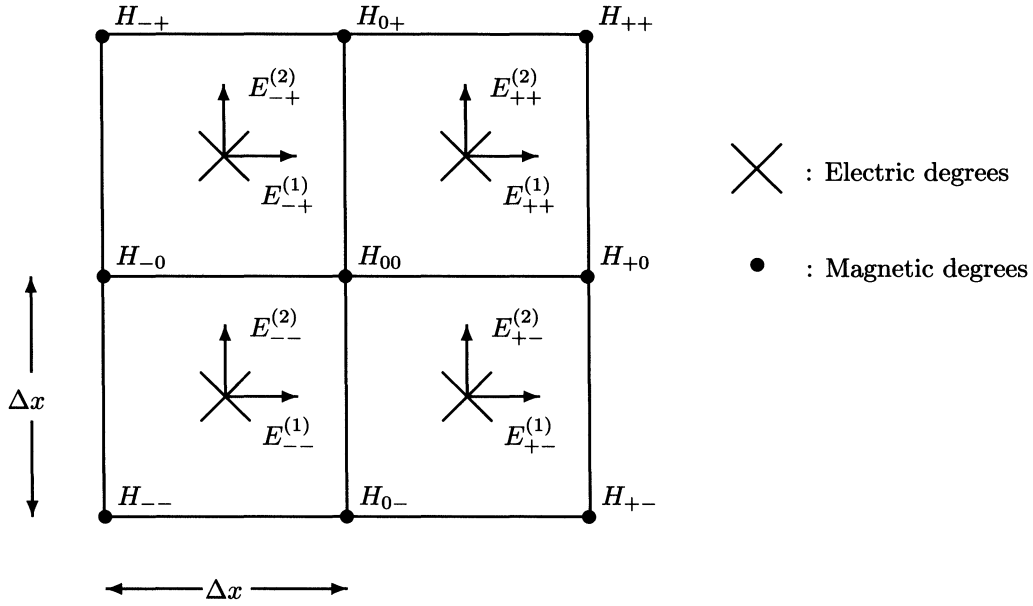


FIG. 1. *A portion of a uniform quadrilateral grid showing the positions of the degrees of freedom for Lee's method. The equations for the indicated degrees of freedom are given in* (29)–(31).

method with the degrees of freedom labeled. If we consider the very special case of (18)–(19) with $\boldsymbol{J} \equiv 0, \sigma \equiv 0, \epsilon = \mu = 1$, and $(U_h^L, V_h^L)$ given by (26) and (28), we obtain the following equations for the degrees of freedom:

$$\frac{d}{dt} E^{(1)}_{++} - \left( \frac{(H_{0+} + H_{++}) - (H_{00} + H_{+0})}{2\Delta x} \right) = 0, \tag{29}$$

$$\frac{d}{dt} E^{(2)}_{++} + \left( \frac{(H_{+0} + H_{++}) - (H_{0+} + H_{00})}{2\Delta x} \right) = 0, \tag{30}$$

$$\begin{aligned} &\frac{d}{dt}\left[ \frac{1}{36}[H_{+-} + H_{++} + H_{--} + H_{-+}] \right. \\ &\qquad \left. + \frac{1}{9}[H_{0-} + H_{-0} + H_{+0} + H_{0+}] + \frac{4}{9} H_{00} \right] \\ &+ \frac{1}{2\Delta x}\left\{ [(E^{(2)}_{++} + E^{(2)}_{+-}) - (E^{(2)}_{-+} + E^{(2)}_{--})] \right. \\ &\qquad \left. - [(E^{(1)}_{++} + E^{(1)}_{-+}) - (E^{(1)}_{+-} + E^{(1)}_{--})] \right\} = 0. \end{aligned} \tag{31}$$

Clearly (29)–(31) are a centered difference approximation to (1)–(2) and thus have local truncation error $O((\Delta x)^2)$ provided $\boldsymbol{E}$ and $H$ are smooth enough. Given the stability result (21), this implies that on a uniform mesh, ECHL converges with error $O((\Delta x)^2)$ at the points indicated in Fig. 1 (convergence is in the discrete $L^2$ norm at each timestep [11]). More precisely, let us define the norms

$$\|u\|_{0,\epsilon} = \sqrt{(\epsilon u, u)} \quad \text{and} \quad \|u\|_{0,\mu} = \sqrt{(\mu u, u)}, \tag{32}$$

and let $\boldsymbol{r}_h \boldsymbol{E} \in U_h^L$ interpolate $\boldsymbol{E}$ at the interpolation points shown in Fig. 1. Let $r_h H \in V_h^L$ be the interpolant for the magnetic field space. Then the stability estimate

(22) and the second-order local truncation error of the method imply that

$$\|(r_h \boldsymbol{E} - \boldsymbol{E}^h)(t)\|_{\epsilon,0} + \|(r_h H - H^h)(t)\|_{\mu,0} = O((\Delta x)^2), \tag{33}$$

provided the initial data is chosen to satisfy (33) at $t = 0$.

In trying to prove convergence on more general domains, we see that ECHL suffers from a big theoretical drawback in that the spaces $(U_h^L, V_h^L)$ do not satisfy an appropriate inf-sup condition and hence ECHL is not included in the general theory of Brezzi [2]. In this context, the inf-sup condition would state that for every nonconstant $H^h \in V_h^L$ (i.e., a function such that $\int_\Omega |\nabla H^h|^2 \, d\boldsymbol{x} \neq 0$) there should exist a function $\phi^h \in U_h^L$ such that $(\vec{\nabla} \times H^h, \phi^h) \neq 0$. However, at least for some meshes, it is easy to construct a function $H^{*h} \in V_h^L$ such that

$$(\vec{\nabla} \times H^{*h}, \phi^h) = 0 \quad \forall \phi^h \in U_h^L, \tag{34}$$

so that the inf-sup condition does not hold. To see this, consider first the reference element $\hat{K} = [0,1] \times [0,1]$. Let $\hat{H}^* \in Q_{11}$ be the bilinear function such that $\hat{H}^*(0,0) = \hat{H}^*(1,1) = 1$ and $\hat{H}^*(1,0) = \hat{H}^*(0,1) = -1$. Direct computation shows that $\vec{\nabla} \times \hat{H}^* = (2-4\hat{x}, -2+4\hat{y})^T$ and hence $\int_{\hat{K}} \vec{\nabla} \times \hat{H}^* \cdot \phi = 0$ for any constant vector $\phi$. For a general mesh, copies of this function can often be used to construct a function $H^{*h} \in V_h^L$ that satisfies (34). For example, on a square domain, meshed with a uniform grid of squares, $H^{*h}$ is the piecewise bilinear function that interpolates $\pm 1$ at the vertices with the values of $+1$ and $-1$ arranged in a checkerboard configuration. We can use $H^{*h}$ to show nonphysical behavior in ECHL. Suppose we solve (21)–(25) with $\boldsymbol{J} \equiv 0$ and $\gamma \equiv 0$ and with initial data

$$\boldsymbol{E}_0^h = 0, \qquad H_0^h = H^{*h}.$$

Then we see that the solution at later times is given by

$$\boldsymbol{E}^h(t) = 0, \qquad H^h(t) = H^{*h}.$$

Given the perfect conducting boundary condition, this solution is nonphysical. Of course, $H^{*h}$ oscillates on a wavelength of order $h$ and thus it is not surprising that the numerical method propagates this high frequency solution poorly. In §4, we use a dispersion analysis to investigate the accuracy of wave propagation as a function of frequency and wavelength for each of the methods discussed in this paper. The lack of an inf-sup condition makes general error estimation difficult and it is not proven, to our knowledge, that ECHL is convergent on general grids. Nevertheless, for smooth data it is possible for the method to converge and work well in practice, as we shall see.

The next method is based on the same variational formulation as ECHL, but the space for the electric field has been modified so that the inf-sup condition holds.

**3.2. The MECHL method.** This method is based on (18)–(20) and is obtained by restricting the three-dimensional method of [12] to two dimensions by assuming $H$ is $z$-polarized and independent of $z$. Let us denote the spaces for the method by $U_h^M$ and $V_h^M$. The method has the same space for the magnetic field as is used by Lee and Madsen, thus $V_h^M = V_h^L$. The electric field space $U_h^M$ is the space $U_h^L$ of ECHL augmented by some linear terms. Therefore, we refer to this method as the MECHL (modified ECHL).

To define the electric field space, denoted $U_h^M$, we first give the reference element $(\hat{K}, P_{\hat{K}}, \Sigma_{\hat{K}})$. Again $\hat{K}$ is given by (23), and

$$P_{\hat{K}} = \{\boldsymbol{p} \mid \boldsymbol{p} \in Q_{10} \times Q_{01}\},$$
$$\Sigma_{\hat{K}} = \left\{ \boldsymbol{p} \cdot \hat{\boldsymbol{n}}(\boldsymbol{b}_i)\, 1 \le i \le 4 \mid, \quad \text{where } \boldsymbol{b}_i = \frac{\boldsymbol{a}_i + \boldsymbol{a}_{i+1}}{2} (\boldsymbol{a}_5 = \boldsymbol{a}_1) \right\}.$$

In these definitions $\hat{\boldsymbol{n}}$ is the unit outward normal to $\hat{K}$. This choice of $P_{\hat{K}}$ is made since $\vec{\nabla} \times Q_{11} \subset Q_{10} \times Q_{01}$, and we want to construct $U_h^M$ such that $\nabla \times V_h^M \subset U_h^M$. Since $V_h^M$ is an isoparametric space, this implies some care with the way that $U_h^M$ is obtained from the reference element. By computing $\vec{\nabla} \times \psi$ for $\psi \in V_h^M$, we find that the correct choice is

$$U_h^M = \{\boldsymbol{u}^h \mid \boldsymbol{u}^h|_K = ((\det \boldsymbol{J}_K)^{-1} \boldsymbol{J}_K \hat{\boldsymbol{u}}_K) \circ F_K^{-1} \text{ for some } \hat{\boldsymbol{u}}_K \in Q_{10} \times Q_{01} \quad \forall K \in \tau_h\}. \tag{35}$$

This space has as degrees of freedom $\boldsymbol{u}^h \cdot \boldsymbol{n}$ at the midpoint of each edge of each element. However, since we wish to allow $\epsilon$, the permittivity, to be discontinuous, we do not require continuity of $\boldsymbol{u}^h \cdot \boldsymbol{n}$ across element boundaries. So the actual degrees of freedom on element $K$ are

$$\lim_{\substack{\boldsymbol{x} \to \boldsymbol{b} \\ \boldsymbol{x} \in K}} \boldsymbol{u}^h(\boldsymbol{x}) \cdot \boldsymbol{n}_K(\boldsymbol{b}),$$

where $\boldsymbol{n}_K$ is the outward normal to $K$ and $\boldsymbol{b}$ is the midpoint of an edge. If we know that $\epsilon$ is continuous, we can decrease the dimension of $U_h^M$ by enforcing continuity of normal components across element boundaries. In that case, $U_h^M$ becomes the lowest-order Raviart–Thomas divergence-conforming space [14] and MECHL becomes essentially the method of Adam et al. [1] (but without mass lumping and with different boundary conditions).

The transformation used in (35) to obtain $\boldsymbol{u}^h|_K$ from $\hat{\boldsymbol{u}}$ implies that

$$\nabla \times V_h^M \subset U_h^M \tag{36}$$

so that the analysis of Monk [12] holds and we can be sure that, on a general mesh, the method converges with error

$$\|(\boldsymbol{E} - \boldsymbol{E}^h)(t)\|_{0,\epsilon} + \|(H - H^h)(t)\|_{0,\mu} = O(h), \tag{37}$$

provided the standard assumptions on isoparametric meshes hold [4], the exact solution is sufficiently smooth, and the initial data for the discrete problem satisfies (37). This is an optimal global estimate since $U_h^M$ does not contain all vector linear polynomials on the reference element.

Note also that in the special case when $\epsilon = \mu = 1$ (or constant) and $\sigma \equiv 0, \boldsymbol{J} \equiv 0$, the fact that $\nabla \times V_h^M \subset U_h^M$ implies that (1) is satisfied pointwise exactly. In particular, we have that

$$\boldsymbol{E}_t^h = \vec{\nabla} \times H^h,$$

and hence $\nabla \cdot \boldsymbol{E}_t^h = 0$. Thus if the initial data $\boldsymbol{E}_0^h$ is chosen so that $\nabla \cdot \boldsymbol{E}_0^h$ is defined and $\nabla \cdot \boldsymbol{E}_0^h = 0$ in $\Omega$, then we can be sure that

$$\nabla \cdot \boldsymbol{E}^h = 0$$

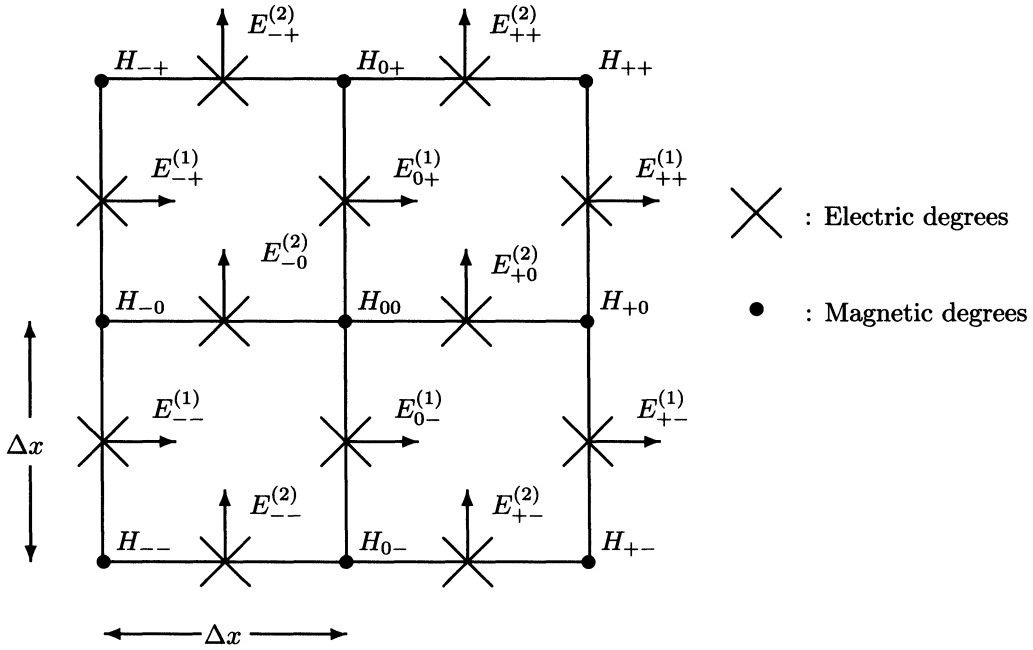


FIG. 2. *The degrees of freedom for* MECHL *on a uniform square grid. In this case we assume that the electric field has continuous normal component across the edge of each element. Thus the electric field degrees of freedom are the normal component of the field at the midpoint of each edge marked* $\times$. *The magnetic degrees of freedom (marked* $\bullet$*) are the same as for* ECHL (*see Fig.* 1).

for all time. Thus in some cases, MECHL allows the exact satisfaction of the equations for the electric field. We remark that $\nabla \cdot \boldsymbol{E}_0^h$ is defined if $\boldsymbol{E}_0^h$ is chosen so that the normal components of $\boldsymbol{E}_0^h$ are continuous across each edge of the mesh [13].

We can also analyze MECHL on a uniform grid. We assume, as before, that $\epsilon = \mu = 1, \sigma \equiv 0, \boldsymbol{J} \equiv 0$, and since $\epsilon$ is continuous we assume that $\boldsymbol{E}^h$ has continuous normal component across each edge of the mesh. The arrangement of degrees of freedom is shown in Fig. 2. On the uniform mesh, we can derive the following equations for the degrees of freedom.

$$\frac{d}{dt} E^{(1)}_{0+} - \frac{H_{0+} - H_{00}}{\Delta x} = 0, \tag{38}$$

$$\frac{d}{dt} E^{(2)}_{+0} + \frac{H_{+0} - H_{00}}{\Delta x} = 0, \tag{39}$$

$$\begin{aligned} &\frac{d}{dt}\left[\frac{1}{36}[H_{++} + H_{--} + H_{+-} + H_{-+}]\right. \\ &\qquad \left. + \frac{1}{9}[H_{-0} + H_{0-} + H_{+0} + H_{0+}] + \frac{4}{9}H_{00}\right] \\ &\quad + \frac{1}{6\Delta x}\left[[(E^{(2)}_{++} + 4E^{(2)}_{+0} + E^{(2)}_{+-}) - (E^{(2)}_{-+} + 4E^{(2)}_{-0} + E^{(2)}_{--})]\right. \\ &\qquad \left. - [(E^{(1)}_{-+} + 4E^{(1)}_{0+} + E^{(1)}_{++}) - (E^{(1)}_{--} + 4E^{(1)}_{0-} + E^{(1)}_{+-})]\right] = 0. \end{aligned} \tag{40}$$

We see that this is another centered finite-difference analogue of (1)–(2) and hence has local truncation error $O((\Delta x)^2)$. Again the stability of the method implies that

in the weighted discrete $L^2$ norm (cf. (32) and (33)), the order of convergence for the method is $O((\Delta x)^2)$ at the points shown in Fig. 2. The precise form of the estimate is exactly as given in (33), provided $\boldsymbol{r}_h$ and $r_h$ are taken to be the interpolation operators for $U_h^M$ and $V_h^M$, respectively. This is a superconvergence result since the order at selected points is one greater than the global error expected using $U_h^M$.

By comparison, a Yee-type [18] finite-difference scheme for this problem, with the grid and degrees of freedom shown in Fig. 2, would be

$$\frac{d}{dt} E_{0+}^{(1)} - \frac{H_{0+} - H_{00}}{\Delta x} = 0, \tag{41}$$

$$\frac{d}{dt} E_{+0}^{(2)} + \frac{H_{+0} - H_{00}}{\Delta x} = 0, \tag{42}$$

$$\frac{d}{dt} H_{00} + \frac{1}{\Delta x}\left[E_{+0}^{(2)} - E_{-0}^{(2)} - [E_{0+}^{(1)} - E_{0-}^{(1)}]\right] = 0. \tag{43}$$

Thus we see that the MECHL finite-element method on a uniform grid is just an averaged version of the Yee method.

**3.3. Nédélec's method.** This method is based on (14)–(17) and was first proposed in [13] (in three dimensions). The version presented here is modified to allow a discontinuity in $\mu$. The magnetic field space is simple, but the electric field space is a subspace of $H(\mathrm{curl};\Omega)$. Nédélec [13] shows that for a finite-element space $U_h^N$ to be a subspace of $H(\mathrm{curl};\Omega)$ it suffices that functions in $U_h^N$ have continuous tangential component across edges in the mesh (i.e., $\boldsymbol{n} \times \boldsymbol{u}^h$ continuous across each internal edge in the mesh for each $\boldsymbol{u}^h \in U_h^N$). Following Nédélec [13] we define the reference element as follows:

$$\begin{aligned}
&\hat{K} \equiv \text{unit square} \quad (\text{see (23)}),\\
&P_{\hat{K}} \equiv Q_{01} \times Q_{10},\\
&\Sigma_{\hat{K}} \equiv \left\{ (\hat{\boldsymbol{u}} \cdot \hat{\boldsymbol{t}})(\hat{\boldsymbol{b}}_i) \mid \boldsymbol{b}_i = \frac{\hat{\boldsymbol{a}}_i + \hat{\boldsymbol{a}}_{i+1}}{2},\ 1 \le i \le 4, \right.\\
&\qquad\qquad \left. \text{where } \boldsymbol{a}_5 = \boldsymbol{a}_1 \text{ and } \hat{\boldsymbol{t}} \text{ is the unit tangent to } \partial\hat{K} \right\}.
\end{aligned}$$

Nédélec [13] shows that a finite-element space constructed from this reference element is $H(\mathrm{curl};\Omega)$-conforming (strictly speaking, Nédélec's results are for $\mathbb{R}^3$ but can be easily reinterpreted for $\mathbb{R}^2$). Care must be taken in the isoparametric method to ensure continuity of tangential components. Thus Nédélec shows that

$$\begin{aligned}
U_h^N = \{\boldsymbol{u}^h \in H(\mathrm{curl};\Omega) | \boldsymbol{u}^h|_K = (\boldsymbol{J}_K^{-T} \hat{\boldsymbol{u}}_K) \circ F_K^{-1},\\
\hat{\boldsymbol{u}}_K \in Q_{01} \times Q_{10} \quad \forall K \in \tau_h\}.
\end{aligned} \tag{44}$$

Using the above space we define

$$U_{h0}^N = \{\boldsymbol{u}^h \in U_h^N \mid \boldsymbol{n} \times \boldsymbol{u}^h = 0 \text{ on } \Gamma\},$$

which can be constructed by enforcing a zero tangential component (zero degree of freedom) on each edge on $\Gamma$. The function $\gamma^h$ required in (16) is the piecewise constant function interpolating $\gamma$ at the midpoint of each boundary edge. Having defined $U_h^N$, we can essentially take $V_h^N$ to be the space of piecewise constants. However, we would like $\nabla \times U_h^N \subset V_h^N$ and thus use an isoparametric mapping of the constant space:

$$V_h^N = \{v^h \mid v^h|_K = ((\det \boldsymbol{J}_K)^{-1} \hat{v}_K) \circ F_K^{-1}, \quad \hat{v}_K \in Q_{00} \quad \forall K \in \tau_h\}. \tag{45}$$

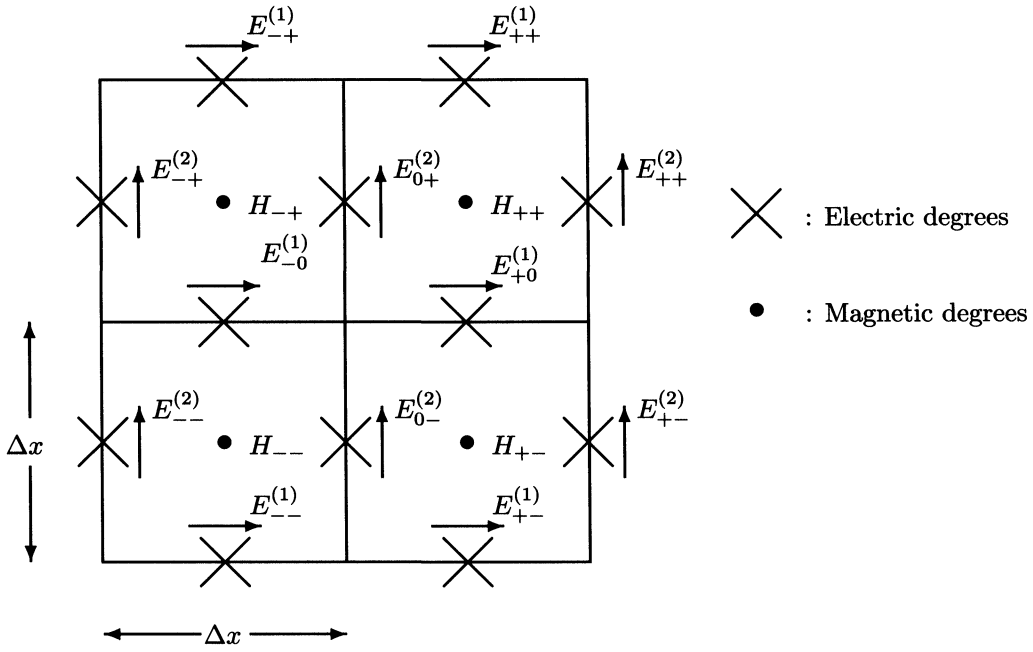


FIG. 3. *The degrees of freedom for* $\mathrm{EL}_N\mathrm{HC}$. *Electric field degrees of freedom are the tangential components of the electric field at the midpoint of each edge of the mesh, marked* $\times$ *(the nearby arrows show the direction of the degree of freedom at the interpolation point). The magnetic field has degrees of freedom marked* $\bullet$.

Since $\nabla \times U_h^N \subset V_h^N$, we know that, provided $\mu$ is constant (as it is in all the examples here),

$$\mu H_t^h + \nabla \times \boldsymbol{E}^h = 0$$

pointwise in $\Omega$, and the magnetic field equation is satisfied exactly. Since the electric field is approximated by Nédélec's linear elements, we refer to this method as $\mathrm{EL}_N\mathrm{HC}$. We emphasize that this is a different method than the method ELHC in [9], which is based on standard continuous linear elements.

This method is analyzed in [11] for the full Maxwell system in three space dimensions. In general, the method has global $L^2$ error at least $O(h)$ (see (37) for a more precise statement). Also in [11], we prove higher-order convergence rates at special points when the mesh is uniform. This is done as follows. If we use the notation in Fig. 3, we can derive the equations satisfied by the degrees of freedom as follows:

$$\frac{d}{dt}\frac{1}{6}\left\{E^{(1)}_{++} + 4E^{(1)}_{+0} + E^{(1)}_{+-}\right\} - \frac{H_{++} - H_{+-}}{\Delta x} = 0, \tag{46}$$

$$\frac{d}{dt}\frac{1}{6}\left\{E^{(2)}_{++} + 4E^{(2)}_{0+} + E^{(2)}_{-+}\right\} + \frac{H_{++} - H_{-+}}{\Delta x} = 0, \tag{47}$$

$$\frac{d}{dt} H_{++} + \frac{1}{\Delta x}\left\{(E^{(2)}_{++} - E^{(2)}_{0+}) - (E^{(1)}_{++} - E^{(1)}_{+0})\right\} = 0. \tag{48}$$

Again, we see that the method has local truncation error $O((\Delta x)^2)$ and the stability result (22) implies convergence in a suitable weighted discrete $L^2$ norm at the mesh points in the same sense as for the two previous methods discussed in this section [11].

For this grid the Yee finite-difference scheme [18] is

$$\frac{d}{dt}E^{(1)}_{+0} - \frac{H_{++} - H_{+-}}{\Delta x} = 0,$$
$$\frac{d}{dt}E^{(2)}_{0+} + \frac{H_{++} - H_{-+}}{\Delta x} = 0,$$
$$\frac{d}{dt}H_{++} + \frac{1}{\Delta x}\left\{(E^{(2)}_{++} - E^{(2)}_{0+}) - (E^{(1)}_{++} - E^{(1)}_{+0})\right\} = 0,$$

which we see is just (41)–(43) with a renaming of nodes. Thus, on a uniform grid, both MECHL and EL$_N$HC are essentially averaged Yee schemes.

**3.4. Timestepping.** In contrast to the rather unusual finite-element spaces used in the spatial discretization, we use the standard leapfrog method to discretize in time [18]. Each of the methods outlined above gives rise to a matrix problem of the following type. Let $(\vec{E}(t), \vec{H}(t))$ be the vectors of free degrees of freedom for the electric and magnetic field, respectively. Then using either (14)–(17) or (18)–(20), $(\vec{E}(t), \vec{H}(t))$ satisfies a matrix problem of the form

$$M^{\epsilon}_{uu}\frac{d\vec{E}}{dt} + M^{\sigma}_{uu}\vec{E} - C_{uv}\vec{H} = \vec{G}, \tag{49}$$

$$M^{\mu}_{vv}\frac{d\vec{H}}{dt} + [C_{uv}]^T\vec{E} = \vec{F}, \tag{50}$$

where $\vec{G}$ and $\vec{F}$ are vectors taking into account boundary data and the applied currents. For example, in the ECHL (respectively, MECHL) methods (see (25))

$$\begin{aligned}
[M^{\epsilon}_{uu}]_{ij} &= \textstyle\int_\Omega \epsilon\boldsymbol{\phi}_i\boldsymbol{\phi}_j dA, && 1 \le i,j \le N_E,\\
[M^{\sigma}_{uu}]_{ij} &= \textstyle\int_\Omega \sigma\boldsymbol{\phi}_i\boldsymbol{\phi}_j dA, && 1 \le i,j \le N_E,\\
[C_{uv}]_{ij} &= \textstyle\int_\Omega (\vec{\nabla}\times\psi_j)\boldsymbol{\phi}_i dA, && 1 \le j \le N_H, \quad 1 \le i \le N_E,\\
[\vec{G}]_i &= \textstyle\int_\Omega \boldsymbol{J}\boldsymbol{\phi}_i dA, && 1 \le i \le N_E,\\
[M^{\mu}_{vv}]_{ij} &= \textstyle\int_\Omega \mu\psi_i\psi_j dA, && 1 \le i,j \le N_H,\\
[\vec{F}]_j &= \textstyle\int_\Gamma \gamma\psi_j dA, && 1 \le j \le N_H,
\end{aligned}$$

where $\{\phi_i\}_{i=1}^{N_E}$ is a basis for $U^L_h$ (respectively, $U^M_h$) and $\{\psi_i\}_{i=1}^{N_E}$ is a basis for $V^L_h$ (respectively, $V^M_h$). Similar definitions hold for the Nédélec method after allowing for the fact that boundary degrees of freedom for $U^N_h$ are specified via the boundary data (16). The fully discrete scheme is to compute a sequence $\{\vec{E}^n, \vec{H}^{n+1/2}\}_{n=0}^{\infty}$ that approximates $\{\vec{E}(t_n), \vec{H}(t_{n+1/2})\}_{n=1}^{\infty}$, where $t_n = n\Delta t$ and $t_{n+1/2} = (n+1/2)\Delta t$. Given $(\vec{E}^n, \vec{H}^{n+1/2})$, we compute $(\vec{E}^{n+1}, \vec{H}^{n+3/2})$ by solving the system

$$M^{\epsilon}_{uu}\left(\frac{\vec{E}^{n+1} - \vec{E}^n}{\Delta t}\right) + M^{\sigma}_{uu}\left(\frac{\vec{E}^{n+1} + \vec{E}^n}{2}\right) - C_{uv}\vec{H}^{n+1/2} = \vec{G}^{n+1/2} \tag{51}$$

where $\vec{G}^{n+1/2} = \vec{G}(t_{n+1/2})$, then solving

$$M^{\mu}_{vv}\left(\frac{\vec{H}^{n+3/2} - \vec{H}^{n+1/2}}{\Delta t}\right) + [C_{uv}]^T\vec{E}^{n+1} = \vec{F}^{n+1}. \tag{52}$$

For ECHL, $M^{\epsilon}_{uu}$ and $M^{\sigma}_{uu}$ are diagonal, while for MECHL they are block diagonal (with $4 \times 4$ diagonal blocks) and thus (51) may be solved rapidly. $M^{\mu}_{vv}$ is sparse (and identical for ECHL and MECHL) and we solve (52) using the preconditioned conjugate gradient method [7], using the mass-lumped matrix as a preconditioner. Precisely, we define the diagonal matrix $\overline{M}^{\mu}_{vv}$ with diagonal entry $[\overline{M}^{\mu}_{vv}]_i$ by

$$[\overline{M}^{\mu}_{vv}]_i = \sum_{j=1}^{N_H} [M^{\mu}_{vv}]_{ij},$$

and then solve

$$C\vec{Y} = (\overline{M}^{\mu}_{vv})^{-1/2} \left( \vec{F}^{n+1} - [C_{uv}]^T \vec{E}^{n+1} \right)$$

where $C = (\overline{M}^{\mu}_{vv})^{-1/2} (M^{\mu}_{vv}) (\overline{M}^{\mu}_{vv})^{-1/2}$, and hence compute

$$\vec{H}^{n+3/2} = \vec{H}^{n+1/2} + \Delta t (\overline{M}^{\mu}_{vv})^{-1/2} \vec{Y}.$$

This method converges rapidly and we always iterate to completion (i.e., so that successive conjugate gradient iterates differ by less than $10^{-6}$ in the $L^2$ norm). In practice, a coarser error tolerance would produce good results.

In the case of the EL$_N$HC or Nédélec method, $M^{\mu}_{vv}$ is diagonal and hence easily inverted. Then (51) must be solved by conjugate gradients, and we also precondition with the mass-lumped matrix, although on a regular grid this is not necessary. The number of conjugate gradient iterations per step for the preconditioned EL$_N$HC matrix is usually less than for the preconditioned ECHL or MECHL methods. However, for EL$_N$HC, the dimension of $M^{\epsilon}_{uu}$ is approximately the number of edges in the mesh, while for ECHL/MECHL the dimension of $M^{\mu}_{vv}$ is the number of nodes in the mesh. Thus we must solve a larger system when timestepping EL$_N$HC than ECHL/MECHL.

To obtain $\vec{H}^{1/2}$, we use a Runge–Kutta-type method. First, we predict a value for $\vec{E}^{1/4}$ by solving

$$M^{\epsilon}_{uu} \left( \frac{\vec{E}^{1/4} - \vec{E}^0}{(\Delta t)/4} \right) + M^{\sigma}_{uu} \vec{E}^0 - C_{uv} \vec{H}^0 = \vec{J}^0,$$

where $\vec{E}^0$ and $\vec{H}^0$ are obtained by interpolating the initial data. Then we compute $\vec{H}^{1/2}$ by solving

$$M^{\mu}_{vv} \left( \frac{\vec{H}^{1/2} - \vec{H}^0}{(\Delta t)/2} \right) + [C_{uv}]^T \vec{E}^{1/4} = \vec{F}^{1/4}.$$

This procedure produces an $O((\Delta t)^2)$ approximation to $\vec{H}(t_{1/2})$. The timestepping scheme (51)–(52) is an $O((\Delta t)^2)$ scheme locally, and we expect that if $\Delta t/h$ is sufficiently small (a standard CFL condition [15]) the overall method will be stable and second order. On uniform grids, this condition is discussed further in §4. For more general grids and problems, convergence has been confirmed numerically, but has not yet been proven for the methods used in this paper.

**4. Dispersion analysis.** In this section, we assume that $\epsilon$ and $\mu$ are constants (which for simplicity we take to be unity), $\sigma \equiv 0$, $\boldsymbol{J} \equiv 0$. In this case, if $\Omega$ is an infinite

domain (or if $\Omega$ is finite and $\gamma$ chosen appropriately), (1) and (2) have solutions of the form

$$\boldsymbol{E}(\boldsymbol{x},t) = \boldsymbol{E}_0 \exp(i(wt - \boldsymbol{k}\cdot\boldsymbol{x})), \tag{53}$$

$$H(\boldsymbol{x},t) = H_0 \exp(i(wt - \boldsymbol{k}\cdot\boldsymbol{x})), \tag{54}$$

where $\boldsymbol{k}$ is a constant vector. Substituting these solutions into (1) and (2) (recalling $\epsilon = \mu = 1$) shows that $w$ and $\boldsymbol{k}$ are related by the dispersion relation

$$w = |\boldsymbol{k}|, \tag{55}$$

where $|\boldsymbol{k}|$ is the Euclidean norm of $\boldsymbol{k}$ (other solutions are $w = 0$ or $w = -|\boldsymbol{k}|$). The group velocity $\boldsymbol{C}$ is given [17] by

$$\boldsymbol{C} = \nabla_{\boldsymbol{k}} w = \frac{\boldsymbol{k}}{|\boldsymbol{k}|}, \tag{56}$$

and hence regardless of the wave number $|\boldsymbol{k}|$ all plane waves move with the same group speed $|\boldsymbol{C}|$. We can also analyze the dispersion relation for each of the numerical methods under consideration. Such an analysis describes how waves propagate in the numerical method far from boundaries, and gives information on the expected accuracy of the methods [17].

For a dispersion analysis, we assume a uniform grid of square elements of dimension $\Delta x \times \Delta x$ (see Figs. 1–3). We assume an infinite grid, and seek solutions of the discrete equations of the form (53)–(54). First we consider the case of exact integration in time, and start with the ECHL method. Substituting (53) and (54) into (29)–(31) we find that, if $\boldsymbol{E}_0 = (E_0^{(1)}, E_0^{(2)}), \zeta_1 = k^{(1)}\Delta x, \zeta_2 = k^{(2)}\Delta x$, $\eta = w\Delta x$, and

$$\gamma(\zeta_1,\zeta_2) = \frac{4}{9} + \frac{2}{9}(\cos(\zeta_1) + \cos(\zeta_2)) + \frac{1}{18}(\cos(\zeta_1 - \zeta_2) + \cos(\zeta_1 + \zeta_2)), \tag{57}$$

then

$$\begin{pmatrix} \sin\left(\frac{\zeta_2-\zeta_1}{2}\right) + \sin\left(\frac{\zeta_1+\zeta_2}{2}\right) & \sin\left(\frac{\zeta_2-\zeta_1}{2}\right) - \sin\left(\frac{\zeta_2+\zeta_1}{2}\right) & \eta\,\gamma(\zeta_1,\zeta_2) \\ \eta & 0 & \sin\left(\frac{\zeta_2-\zeta_1}{2}\right) + \sin\left(\frac{\zeta_2+\zeta_1}{2}\right) \\ 0 & \eta & -\sin\left(\frac{\zeta_1-\zeta_2}{2}\right) - \sin\left(\frac{\zeta_1+\zeta_2}{2}\right) \end{pmatrix} \cdot \begin{pmatrix} E_0^{(1)} \\ E_0^{(2)} \\ H_0 \end{pmatrix} = \begin{pmatrix} 0 \\ 0 \\ 0 \end{pmatrix}. \tag{58}$$

For (58) to have a nontrivial solution, the determinant of the matrix must be zero. This defines $\eta$ as a function of $(\zeta_1,\zeta_2)$. If $\eta^{\circ}_{ECHL}$ denotes the positive solution, we find that

$$\eta^{\circ}_{ECHL}(\zeta_1,\zeta_2) = \left\{ \frac{6\sqrt{\sin^2\left(\frac{\zeta_1-\zeta_2}{2}\right) + \sin^2\left(\frac{\zeta_1+\zeta_2}{2}\right)}}{\sqrt{8 + 4\cos(\zeta_2) + \cos(\zeta_1-\zeta_2) + 4\cos(\zeta_1) + \cos(\zeta_1+\zeta_2)}} \right\} \tag{59}$$

(other solutions are $\eta = 0$ or $\eta$ is the negative of the above expression). Hence, depending on the magnitude and direction of $\boldsymbol{k}$, the numerically computed wave

possesses an erroneous phase. This implies that a plane wave of the form (53) and (54) generally moves in the wrong direction at the wrong speed. Of course if $|\boldsymbol{\zeta}|$ is small, the frequency $w_{ECHL}$ for ECHL with exact time integration is

$$w^{\circ}_{ECHL}(\zeta_1,\zeta_2,\Delta x) \equiv \frac{\eta^{\circ}_{ECHL}(\zeta_1,\zeta_2)}{\Delta x} \sim \sqrt{\frac{\zeta_1^2+\zeta_2^2}{(\Delta x)^2}} = |\boldsymbol{k}|,$$

so that waves with a sufficiently long wavelength compared to the grid move with essentially the correct phase. To derive the frequency $w$ for the fully discrete scheme, we see that discretization in time corresponds to replacing $\eta$ in (58) by $2\frac{\Delta x}{\Delta t}\sin\left(\frac{w\Delta t}{2}\right)$, and thus if we denote the frequency for the fully discrete scheme by $w^{\Delta t}_{ECHL}(\zeta_1,\zeta_2,\lambda,\Delta t)$ and let $\lambda = \Delta t/\Delta x$, we find that

$$w^{\Delta t}_{ECHL}(\zeta_1,\zeta_2,\lambda,\Delta t) = \frac{2}{\Delta t}\sin^{-1}\left(\frac{\lambda\eta^{\circ}_{ECHL}(\zeta_1,\zeta_2)}{2}\right) \tag{60}$$

and the group velocity

$$\boldsymbol{C}^{\Delta t}_{ECHL}(\zeta_1,\zeta_2,\lambda) = \frac{2}{\lambda}\nabla_{\zeta}\left[\sin^{-1}\left(\frac{\lambda\eta^{\circ}_{ECHL}(\zeta_1,\zeta_2)}{2}\right)\right]. \tag{61}$$

In Fig. 4 we show a plot of $|\boldsymbol{C}^{\Delta t}_{ECHL}-\boldsymbol{C}|$ as a function of $\boldsymbol{\zeta}\in[0,\pi]\times[0,\pi]$ (higher values of $\boldsymbol{\zeta}$ are aliased onto the grid [17]). $\boldsymbol{C}^{\Delta t}_{ECHL}$ depends only on $\lambda = \Delta t/\Delta x$, not $\Delta t$ or $\Delta x$ individually, and we choose $\lambda = 0.25$ in accordance with later numerical results (graphs for smaller $\lambda$ are similar). The shaded area is where $|\boldsymbol{C}^{\Delta t}_{ECHL} - \boldsymbol{C}| < 0.1$, so that for a given $\boldsymbol{k}$, if we choose $\Delta x$ such that $\boldsymbol{k}\Delta x$ lies in the shaded region, we can be sure that the wave will move with a wave speed and direction in error by less than 10 percent. A diagram like Fig. 4 can be invaluable for choosing step sizes.

Note also that $\lambda$ must be chosen sufficiently small that

$$\lambda\left(\max_{(\zeta_1,\zeta_2)\in[0,\pi]\times[0,\pi]}|\eta^{\circ}_{ECHL}(\zeta_1,\zeta_2)|\right) \le 2, \tag{62}$$

so that $w^{\Delta t}_{ECHL}$ is real. This implies the condition that

$$\lambda \le \frac{2}{\sqrt{12}} \simeq 0.577\cdots. \tag{63}$$

With mass lumping, an examination of the stencil for ECHL suggests a CFL condition $\lambda \le 1$, but this CFL condition is not correct when the full finite-element mass matrix is used. Thus for the split-step, mixed, finite-element methods considered here some extra care is needed to ensure stability (the condition $\lambda \le 0.577\cdots$ has been checked numerically, and gives an accurate picture of stability for ECHL applied to boundary value problems on a uniform grid (see §5.1)).

We can perform the same dispersion analysis on EL$_N$HC and MECHL. Not surprisingly, these methods have identical dispersion relations (when $\epsilon = \mu = 1$) since both methods are restrictions of three-dimensional methods based on the same spaces (cf. [13] and [11]). Hence we need only analyze EL$_N$HC. In this case the matrix corresponding to (58) is

$$\begin{pmatrix} 2\sin\left(\frac{\zeta_2}{2}\right) & -2\sin\left(\frac{\zeta_1}{2}\right) & \eta \\ \eta\left(\frac{4+2\cos(\zeta_2)}{6}\right) & 0 & 2\sin\left(\frac{\zeta_2}{2}\right) \\ 0 & \eta\left(\frac{4+2\cos(\zeta_1)}{6}\right) & -2\sin\left(\frac{\zeta_1}{2}\right) \end{pmatrix},$$

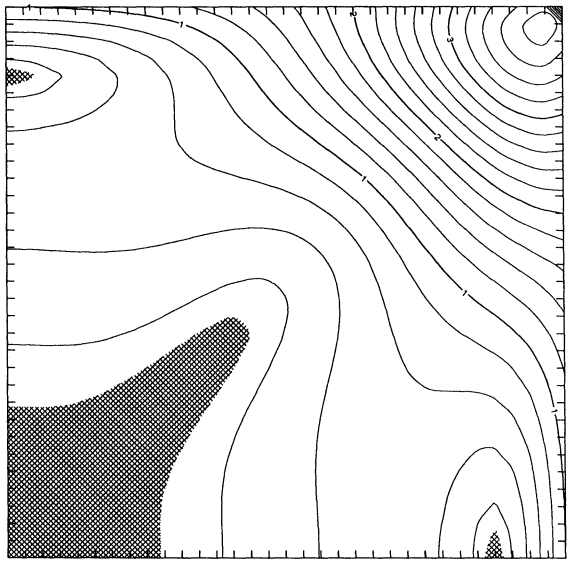


(a)

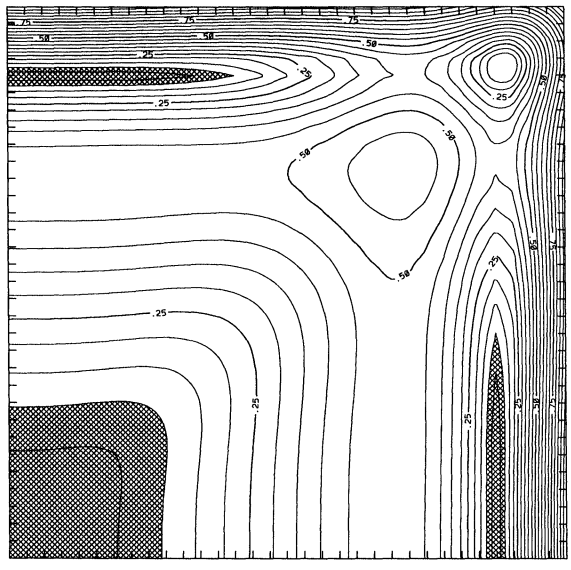


(b)

FIG. 4. *Graphs of the error in the group velocity for* $k\Delta x \in [0,\pi] \times [0,\pi]$. *We show contours of* $|C^{\Delta t} - C|$ *where* $C^{\Delta t}$ *is the numerical group velocity and* $C$ *is the exact group velocity. The shaded region is the region in which* $|C^{\Delta t} - C| < 0.1$. *All three methods have the same dispersion behavior for waves oriented along grid lines, and this implies that the worst-case error for a particular* $|k|\Delta x$ *is the same for each method.* (a) *The group velocity error for* ECHL. *For values of* $|k|\Delta x \sim \pi$ *the group velocity can be in error by up to about* 400 *percent.* (b) *The group velocity error for* MECHL *and* $\mathrm{EL}_N\mathrm{HC}$. *In this case the maximum error is less than for* ECHL. *The error contours for* MECHL/$\mathrm{EL}_N$HC *are more nearly circular than for* ECHL, *implying less grid anisotropy.*

and thus

$$\eta^{\circ}_{EL_NHC}(\zeta_1,\zeta_2) = 2\sqrt{3}\sqrt{\frac{2\sin^2\left(\frac{\zeta_1}{2}\right)+\cos(\zeta_2)\sin^2\left(\frac{\zeta_1}{2}\right)+2\sin^2\left(\frac{\zeta_2}{2}\right)+\cos(\zeta_1)\sin^2\left(\frac{\zeta_2}{2}\right)}{4+2\cos(\zeta_1)+2\cos(\zeta_2)+\cos(\zeta_1)\cos(\zeta_2)}}.$$

The condition corresponding to (63) is

$$\lambda \le 2/\sqrt{24}.$$

For the fully discrete method, $w^{\Delta t}_{EL_NHC}$ and $\boldsymbol{C}^{\Delta t}_{EL_NHC}$ are given by the analogues of (60) and (61). In Fig. 4(b) we show $|\boldsymbol{C}^{\Delta t}_{EL_NHC} - \boldsymbol{C}|$ against $(\zeta_1,\zeta_2)$ and again shade the region with less than 10 percent error. Notice that the EL$_N$HC, ECHL, and MECHL methods have the same dispersion behavior for waves with $\boldsymbol{k} = (k_1, 0)$ or $\boldsymbol{k} = (0, k_2)$ (i.e., parallel to grid lines). This is because MECHL and ECHL are identical schemes in these cases (see (29)–(31), (38)–(40)), and MECHL and EL$_N$HC are based on the same spaces (but used in different ways) in three dimensions.

Clearly, from Fig. 4, the area in the $(\zeta_1,\zeta_2)$ plane for which the numerical group velocity is in error by less than 10 percent is larger for ECHL than MECHL or EL$_N$HC. On the other hand, the error contours for MECHL/EL$_N$HC are more nearly circular than for ECHL, implying less grid anisotropy. Furthermore, the maximum error for MECHL and EL$_N$HC is approximately 100 percent, whereas that for ECHL is 400 percent. Thus ECHL will cause much worse dispersion for very high frequency waves than either MECHL or EL$_N$HC. In general, we must choose a grid on the basis of the worst-case behavior of the method. This occurs in all three methods for waves along the coordinate axis, and is identical for the three methods.

Since the worst case for plane wave propagation is for waves along a grid line, we can gain useful information on error by considering a one-dimensional plot of group velocity error, as shown in Fig. 5. Here we consider waves with wave number $\boldsymbol{k} = (k_1, 0)$ moving along the $x$-axis. We plot group velocity error against number of grid cells per half wave length defined by $N_p = \pi/(k_1\Delta x)$. This graph implies that for an error of 10 percent in the group velocity, we need about eight grid cells per wavelength. For more complex waves (i.e., wave consisting of a superposition of plane waves), we can still use Fig. 5 by considering the plane wave components separately.

On the basis of dispersion, it is difficult to choose between the three methods. In addition, in real problems the mesh is not uniform, the coefficients not constant, and boundary conditions are important. We investigate these problems in §5 using essentially the same numerical examples as [9].

All algebra in the preceding section was manipulated using Mathematica.

**5. Numerical results.** In this section, we further compare the three finite-element methods described in §3 by applying them to selected numerical examples. The examples are all taken from [9].

**5.1. Plane wave propagation.** We shall compare the numerical solution of a simple wave propagation problem with the exact solution. We choose the functions in Maxwell's equations as follows: $\epsilon = \mu = 1$, $\sigma = 0$, and $\boldsymbol{J} = 0$. Then an exact solution of Maxwell's equations (on the entire plane) is

$$\boldsymbol{E}_e(\boldsymbol{x},t) = \begin{pmatrix} -k_2 \\ k_1 \end{pmatrix} g(t - \boldsymbol{k}\cdot\boldsymbol{x}),$$
$$H_e(\boldsymbol{x},t) = g(t - \boldsymbol{k}\cdot\boldsymbol{x}),$$

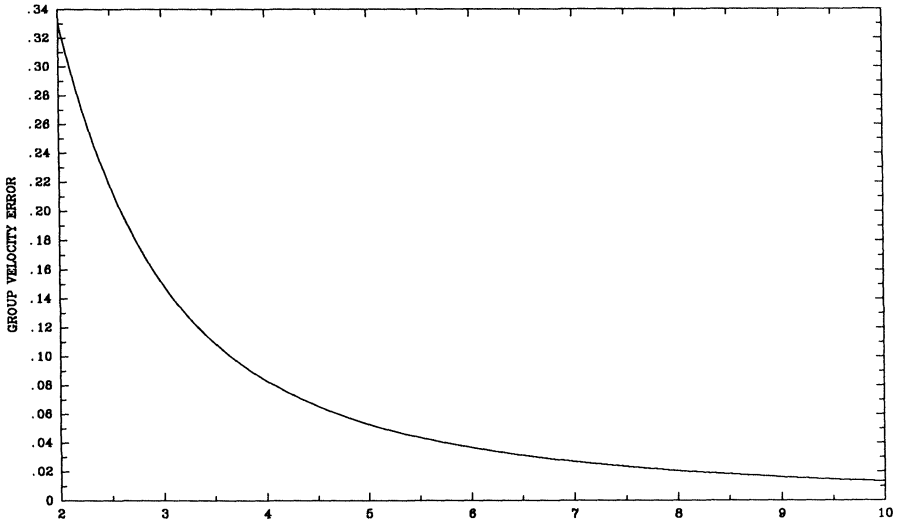


FIG. 5. *A graph of the error in the group velocity for a wave traveling along the $x$-axis with wave number $k = (k_1, 0)$. The error is plotted against number of grid blocks per half wave length defined as $N_p = \pi/(k_1 \Delta x)$. The* CFL *number $\lambda = 0.25$. A wave parallel to a grid direction is the worst case for all three methods. This graph can be used to select the grid size.*

where we take $\boldsymbol{k} = (\cos(1), \sin(1))$ and

$$g(s) = \begin{cases} \frac{\exp(-10(s-1)^2) - \exp(-10)}{1 - \exp(-10)}, & 0 \le s \le 2, \\ 0, & s > 2 \text{ or } s < 0. \end{cases} \tag{64}$$

We choose a finite domain $\Omega = [0,2] \times [0,2]$ and take $\boldsymbol{E}_0 = 0$, $H_0 = 0$, and $\boldsymbol{J}_0 = 0$. The boundary data is chosen consistent with the above exact solution so that $\gamma = \boldsymbol{n} \times \boldsymbol{E}_e$. We discretize the problem using a uniform grid on $\Omega = [0,2] \times [0,2]$ with $N$ subintervals on each edge (thus $N^2$ quadrilaterals). In this case $\Delta x = 2/N$, $h = \sqrt{2}\Delta x$, and we choose the CFL parameter $\lambda = \Delta t / \Delta x = 0.25$. For each method, and a variety of $N$, we integrate until $t = 2$, and then compute the relative discrete $L^2$ norm error in the magnetic field $H$ (for simplicity). Thus we compute

$$\|(H_e - H^h)(t)\|_{L^2,h} = \sqrt{\sum_{i=1}^{N_H} |H_e(\boldsymbol{x}_i, t) - H^h(\boldsymbol{x}_i, t)|^2}$$

at $t = 2$ where $\boldsymbol{x}_i$ is the $i$th node if using ECHL or MECHL, or the centroid of the $i$th quadrilateral if using EL$_N$HC. Then we define

$$\|H_e - H^h\|_{\text{rel}} = \frac{\|H_e - H^h\|_{L^2,h}}{\|H_e\|_{L^2,h}}. \tag{65}$$

A plot of error against $N$ and error against CPU time (on a SUN SparcStation 1) is shown in Fig. 6. The plot of error against $N$ confirms that on a uniform grid all three

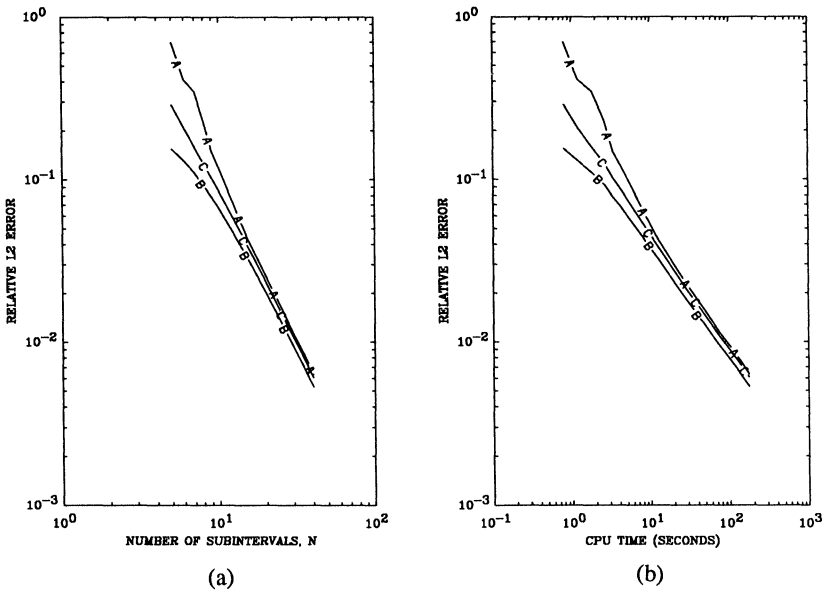


FIG. 6. *Plots of error against grid parameter $N$ and* CPU *time for the example in* §5.1. *A plane wave moves across a uniform grid at an angle to the grid lines. The error reported is the relative discrete $L^2$ error given by* (65). *In each case* —A— *denotes* ECHL, —B— *denotes* $\mathrm{EL}_N\mathrm{HC}$, *and* —C— *denotes* MECHL. (a) *A plot of error against $N$. Here $h = 2\sqrt{2/N}$. This graph suggests second-order convergence in the norm of* (65) *for all three methods.* $\mathrm{EL}_N\mathrm{HC}$ *is notably more accurate for coarse meshes.* (b) *A graph of error against* CPU *time (on a* SUN *SparcStation* 1). *Except possibly for very fine grids,* $\mathrm{EL}_N\mathrm{HC}$ *produces a given error in least time (but see* §5.3). *For this example the conjugate gradient method in* $\mathrm{EL}_N\mathrm{HC}$ *was not preconditioned, since satisfactory convergence was seen without preconditioning.*

methods are ultimately second-order convergent at the degrees of freedom (the slope of the graphs is 2). For a given $N$, $\mathrm{EL}_N\mathrm{HC}$ is always the most accurate and ECHL the least accurate. The disparity is particularly obvious for small $N$. In view of the dispersion analysis, the difference between MECHL and $\mathrm{EL}_N\mathrm{HC}$ must be due to the way that the boundary data is imposed. A slightly different picture emerges when we view error against CPU time. For a given error, $\mathrm{EL}_N\mathrm{HC}$ is the most rapid method, but for a very low error (a fine mesh), it appears that ECHL may become the fastest method. Most time is spent in the conjugate gradient solver. ECHL and MECHL solve the same matrix problem, which has about half as many unknowns as $\mathrm{EL}_N\mathrm{HC}$. However, despite preconditioning, the ECHL/MECHL takes approximately twice as many iterations to solve the matrix problem to comparable accuracy.

Using this example, we have also checked the validity of the stability estimates (62) and (63) in the case of a boundary value problem. For the $\mathrm{EL}_N\mathrm{HC}$, scheme (63) implies that $\lambda \leq 2/\sqrt{24}$ is necessary for stability (for the pure initial value problem). When $N = 30$ this implies that $\Delta t \leq 0.0272\cdots$. We find divergence when $\Delta t = 0.029$, but find satisfactory results with $\Delta t = 0.027$ (at least up to time $t = 4$). For ECHL, $\lambda \leq 2/\sqrt{12}$, and hence if $N = 30, \Delta t \leq 0.0385\cdots$. When $\Delta t = 0.04$ the method is unstable, but converges satisfactorily until $t = 4$ when $\Delta t = 0.038$. These

results indicate that (62) and (63) are pertinent to the stability of the boundary value problem.

**5.2. Simple scattering.** In the previous example we used a uniform grid and a plane wave. Our next example uses a nonuniform grid (which is uniform in polar coordinates) and more complex wave motion. Again following [9], we consider an infinite domain problem of scattering of a plane wave off a circular perfect conductor. We consider a plane wave

$$\boldsymbol{E}_i(\boldsymbol{x},t) = \begin{pmatrix} 0 \\ \sqrt{\mu_0/\epsilon_0}\, g((t-(x-0.1)\sqrt{\epsilon_0\mu_0})10^9) \end{pmatrix}, \tag{66}$$

$$H_i(\boldsymbol{x},t) = g((t-(x-0.1)\sqrt{\epsilon_0\mu_0})10^9) \tag{67}$$

(where $g$ is given by (64)) incident on a perfectly conducting circular cylinder of radius 0.1m centered at the origin. We choose

$$\epsilon = \epsilon_0 = 8.85 \times 10^{-12} F/m^2, \qquad \mu = \mu_0 = 1.2566 \times 10^{-6} N/A^2.$$

Using special function theory, an exact solution is available for this problem [8].

For the numerical problem we take an annular domain with inner radius 0.1m and an outer radius of 1.1m. Since the problem is symmetric about the $x$-axis we use the half-domain

$$\Omega = \left\{(x,y) \mid 0.1 < \sqrt{x^2+y^2} < 1.1, y > 0\right\}.$$

On $y = 0$ we impose the symmetry condition $\boldsymbol{n} \times \boldsymbol{E} = 0$, and on $r = 1.1$ we impose the perfect reflecting boundary condition $\boldsymbol{n} \times \boldsymbol{E} = \gamma \equiv 0$. On $r = 0.1$ we impose $\boldsymbol{n} \times \boldsymbol{E} = \gamma \equiv \boldsymbol{n} \times \boldsymbol{E}_i$, which describes how the incident field scatters off a perfect conductor. The boundary condition $\boldsymbol{n} \times \boldsymbol{E} = 0$ on $r = 1.1$ generates spurious reflections for times greater than about time $t = 4$ nanoseconds (ns), so the exact solution is not useful beyond that time. The grid used has mesh points distributed uniformly in the $(r,\theta)$ plane, i.e., the mesh points are $(r_i,\theta_j)$, $0 \le i \le N_r$, $0 \le j \le N_\theta$, where

$$r_i = 0.1 + \frac{i}{N_r} \quad \text{and} \quad \theta_j = \pi \frac{j}{N_\theta}.$$

In Fig. 7, we show the computed and exact solutions at two interpolation points when $N_r = 30$, $N_\theta = 15$, and $\Delta t = 1 \times 10^{-3}$. With the small timestep used here, most of the error is due to spatial discretization. These results can be compared to [9, Fig. 3]. Clearly, all three methods compute reasonable solutions.

Table 1 shows the relative $L_2$ error in space at various times (error defined by (65)). The error ratios are consistent with second-order convergence (the ratios are shown in parentheses in the table). The small timestep $\Delta t = 1 \times 10^{-3}$ is chosen since we wish to focus on spatial error, and numerical experiments show that, with this timestep, the timestepping error is negligible compared to the spatial error. Thus the second-order convergence shown in Table 1 is evidence of second-order convergence in the spatial error. As yet, we have no theory to predict this rate of convergence. However, the fact of second-order convergence at the mesh points is encouraging since the mesh is slightly nonuniform.

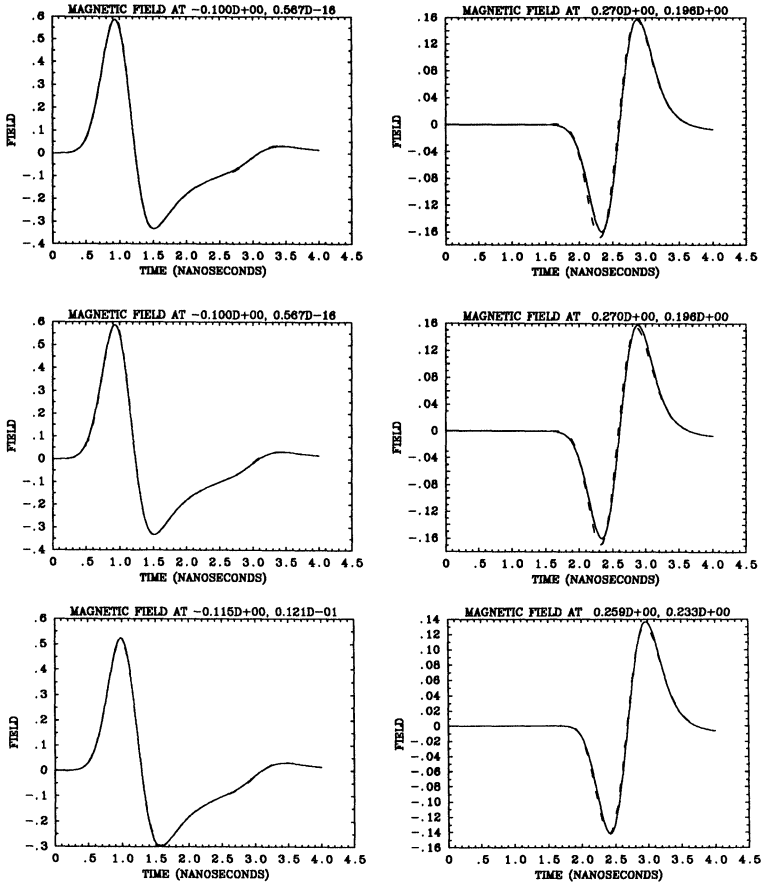


FIG. 7. *A comparison of exact and numerical solution for the simple scattering problem in* §5.2 *at selected spatial points. The exact solution is the solid line and the dashed line shows the computed solution. Here* $N_r = 30$, $N_\theta = 15$, *and* $\Delta t = 1 \times 10^{-3}$. *The coordinates of the spatial points are shown on each plot, and are chosen to be the interpolation point closest to the points A and B in* [9, *Fig.* 2]. *Top row: Results for* ECHL. *Middle row: Results for* MECHL. *Bottom row: Results for* $\mathrm{EL}_N\mathrm{HC}$.

**5.3. Scattering by a dielectric cylinder.** Our final example investigates a very nonuniform mesh and a case in which $\epsilon$ is discontinuous. Again the example is taken from [9]. At a line of discontinuity $L$ separating two regions $\Omega_1$ and $\Omega_2$ with $\epsilon = \epsilon_1$ in $\Omega_1$ and $\epsilon = \epsilon_2$ in $\Omega_2$, we have the continuity condition

$$\epsilon_1(\boldsymbol{n} \cdot \boldsymbol{E})_1 = \epsilon_2(\boldsymbol{n} \cdot \boldsymbol{E})_2, \tag{68}$$

so there is a jump in the normal component of the electric field across $L$ (cf. [9]). If standard continuous finite elements are used to discretize $\boldsymbol{E}$, a complex modification must be made along $L$ to ensure (68) [9]. This modification is not required with any of the methods in this paper, although $L$ must coincide with mesh lines.

To construct an exact solution, we consider the infinite domain-scattering problem

TABLE 1

*Relative $L_2$ error in the magnetic field (as defined by (65)) at various times for two different discretizations of the example in §5.2 (see text for details of the domain and mesh). The numbers in parentheses give the ratio of errors in the table with a ratio of 4 being exactly second-order convergence. A ratio of 3.7 indicates $O(h^{1.9})$ convergence. In this case $\Delta t = 1 \times 10^{-3}$, thus the second-order convergence suggested by this table is the result of second-order convergence of spatial error and not due to the time discretization. By $t = 4$, the solution is polluted by reflections from the artificial boundary.*

| | Time (ns) | ECHL | MECHL | EL$_N$HC |
|---|---|---|---|---|
| $N_r = 30$ | 1 | 0.0222 | 0.0125 | 0.0180 |
| $N_\theta = 15$ | 2 | 0.0638 | 0.0623 | 0.0464 |
| | 3 | 0.143 | 0.157 | 0.107 |
| | 4 | 0.337 | 0.358 | 0.236 |
| $N_r = 60$ | 1 | 0.00547 (4.1) | 0.00338 (3.7) | 0.00485 (3.7) |
| $N_\theta = 30$ | 2 | 0.0161 (4.0) | 0.0164 (3.8) | 0.0124 (3.7) |
| | 3 | 0.0366 (3.9) | 0.0402 (3.9) | 0.0289 (3.7) |
| | 4 | 0.124 (2.7) | 0.128 (2.8) | 0.0982 (2.4) |

in which a plane wave is incident on an inhomogeneous cylinder of radius 0.25m centered at the origin. In this cylinder we assume that the dielectric constant $\epsilon = \epsilon_0/16$ and $\mu = \mu_0$ (see also Fig. 8). This problem can be solved by using special function theory on the infinite domain [8].

To approximate the infinite domain problem, we use the domain shown in Fig. 8. We use the half-domain $y \geq 0$ since the problem is symmetric about the $x$-axis, and use a symmetry boundary condition on the line $y = 0$. Following [9], we take $\boldsymbol{E}_0 = 0$, $H_0 = 0$, $\sigma \equiv 0$, $J \equiv 0$, and $\gamma = 0$ on $\Gamma \backslash \Sigma$. On $\Sigma$ we take

$$\gamma = \begin{cases} 1/2\sqrt{\mu_0/\epsilon_0}(1 - \cos 2\pi t), & 0 \leq t \leq 1, \\ 0, & t > 1. \end{cases}$$

A wave with the cross-section of $\gamma$ above has more slowly decaying harmonics than the incident wave in §5.2. Thus dispersion is more severe for this example than for the example in §5.2.

Using the finite domain shown in Fig. 8(a), we can compute an accurate approximate solution to the infinite domain-scattering problem until reflections from the artificial boundary are significant. We have not attempted to use absorbing boundary conditions on this boundary and instead, to minimize spurious reflections in the output shown in Fig. 9, we compute only up to $t = 6ns$.

We use a mesh similar to the one in [9]. An example is shown in Fig. 8(b) when $N = 16$. In this case $N$ refers to the number of subintervals along the line $x = -1$. Table 2 shows the relative $L^2$ error on the subdomain $\{(x, y) \mid |x| \leq 0.5,\ 0 \leq y \leq 0.5\}$ at various times for $N = 16$ and $N = 32$ ($N = 32$ corresponds to subdividing every quadrilateral in the $N = 16$ mesh into four subquadrilaterals). We compute the error on a subdomain for two reasons: first, we want to investigate error behavior on the nonuniform portion of the mesh; and second, we want to avoid errors due to spurious reflections from the boundary. The timestep used gives an approximate CFL number of 0.25 in the inner circle where $\epsilon = \epsilon_0/16$. The results in Table 2 are consistent with an order convergence of at least $O(h^{1.6})$ for all three methods. It thus appears that three-halfs-order or possibly even second-order superconvergence is seen even on nonuniform meshes and in the presence of material discontinuities. This is unexpected and needs to be justified by further numerical and theoretical investigations. It is possible that for finer meshes the order of convergence would approach first order.

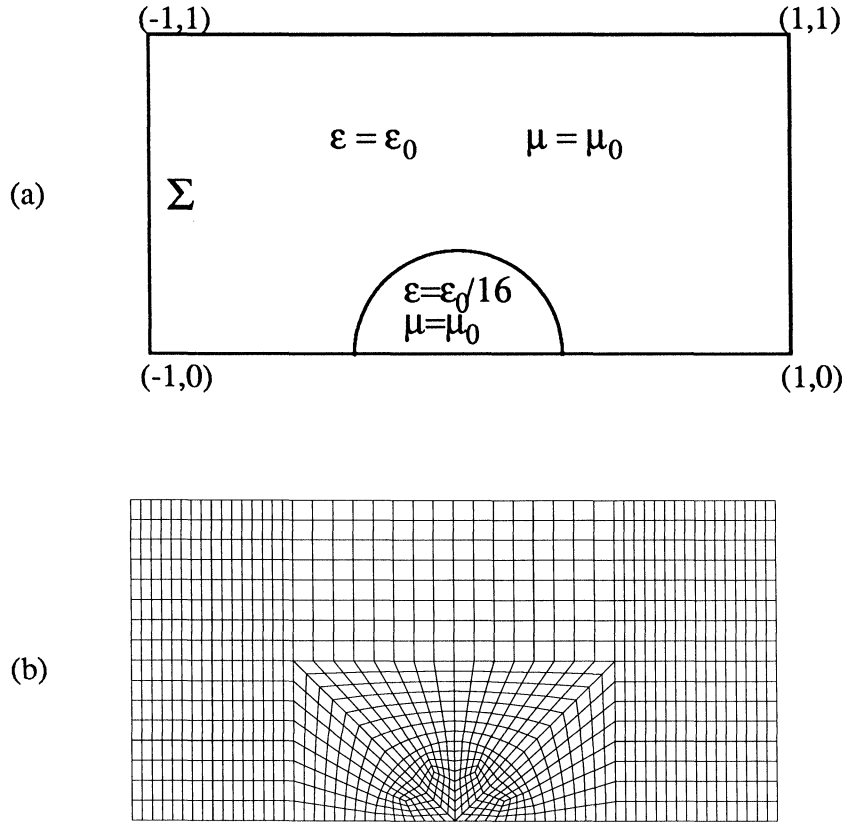


FIG. 8. *The domain $\Omega$ for the example in* §5.3. (a) *We show the domain $\Omega$ indicating the values of the material parameters in each subdomain. $\Sigma$ marks the boundary edge on which inhomogeneous boundary data is specified.* (b) *An example of the mesh. Here $N = 16$ ($N$ is number of subintervals along $x = -1$).*

TABLE 2

*Relative $L_2$ error in the magnetic field (as defined by* (65)*) on the subdomain $\{(x, y) \mid |x| \leq 0.5\ 0 \leq y \leq 1\}$ at various times for two different discretizations of the example in* §5.3 *(see text and Fig. 8 for details of the domain and mesh). In this case the* CFL *number $\lambda$ is approximately* 0.25 *in the inner domain. The numbers in parentheses give the ratio of errors in the table. Errors at all times show faster than $O(h)$ convergence (a decrease of error by a factor of* 3 *is $O(h^{1.6})$) which is unexpected.*

| | Time (ns) | ECHL | MECHL | EL$_N$HC |
|---|---|---|---|---|
| $N = 16$ $\Delta t = 0.001$ | 2 | 0.234 | 0.235 | 0.263 |
| | 3 | 0.226 | 0.268 | 0.215 |
| | 4 | 0.243 | 0.291 | 0.245 |
| | 5 | 0.406 | 0.447 | 0.407 |
| | 6 | 0.551 | 0.545 | 0.383 |
| $N = 32$ $\Delta t = 0.0005$ | 2 | 0.0730 (3.2) | 0.0748 (3.1) | 0.0762 (3.5) |
| | 3 | 0.0635 (3.6) | 0.0757 (3.5) | 0.0635 (3.4) |
| | 4 | 0.0719 (3.4) | 0.0891 (3.3) | 0.0756 (3.2) |
| | 5 | 0.132 (3.1) | 0.163 (2.7) | 0.140 (2.9) |
| | 6 | 0.181 (3.0) | 0.208 (2.6) | 0.135 (2.8) |

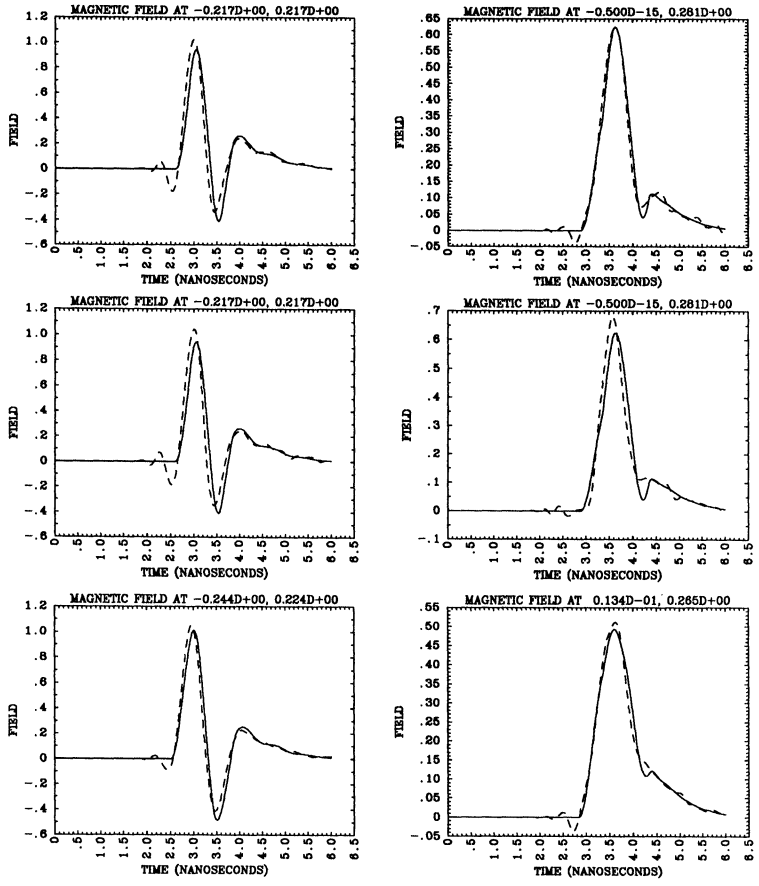


FIG. 9. *A comparison of exact and numerical solution for the simple scattering problem in* §5.3 *at selected spatial points. The exact solution is the solid line and the dashed line shows the computed solution. Here* $N = 16$ *and the* CFL *number for the inhomogeneous cylinder is approximately* 0.25. *The coordinates of the spatial points are shown on each plot, and are chosen to be the interpolation point closest to the points A and B in* [9, Fig. 4]. *Dispersion is visible in all plots, particularly along the leading edge of the wave. Top row: Results for* ECHL. *Middle row: Results for* MECHL. *Bottom row: Results for* $\mathrm{EL}_N\mathrm{HC}$.

Figure 9 shows the results of all three methods when $N = 16$ at two points in the domain. These are the interpolation points closest to the points $A$ and $B$ in [9, Fig. 4]. All three methods give qualitatively similar results. Significant dispersion occurs in the coarsely meshed region above the cylinder shown in Fig. 8(b), but this tends not to effect the solution at the points given in Fig. 9. Clearly, although dispersion is evident, all three methods produce qualitatively similar and reasonable results. In particular, all three methods can handle discontinuous media with no problem.

We have used a significantly smaller timestep in this example compared to that used in [9], and we find that all three methods are unstable with the mesh and time step parameters used in [9]. Note that our implementation of ECHL differs from

that in [9] in that we solve (49) and (50) by conjugate gradients with a stringent stopping tolerance. If the iterative method is only allowed to perform a small number of iterations per timestep, it is possible that this incomplete iteration will smooth the solution and allow longer timesteps.

As a final remark on this example, we note that even with preconditioning, the conjugate gradient scheme for $EL_NHC$ was very slowly convergent for this example (particularly when $N = 32$). In this example, $EL_NHC$ was much slower than ECHL or MECHL.

**6. Conclusions.** The methods under consideration in this paper have quite similar features. All are based on mixed finite-element spaces approximating the full Maxwell system. Moreover, in the examples computed, none of the methods has a decisive edge over the rest. The ECHL method has a larger stability boundary or CFL condition, but is sometimes less accurate than the other methods and suffers from greater grid anisotropy. Generally, the $EL_NHC$ method is most accurate, and MECHL is either more accurate or approximately the same accuracy as ECHL. The state of theory for ECHL is not as well developed as for MECHL or $EL_NHC$, and in all three cases an improved understanding of superconvergence is desirable.

Clearly, a second important area of research is to examine other timestepping methods. The stability condition for these schemes should be better understood, and less restrictive timestepping methods should be investigated (cf. [1]).

All three schemes have three-dimensional counterparts, and the results in this paper and in [9] suggest they will be successful schemes. Given the ease of implementation of methods with natural boundary conditions, ECHL or MECHL may be preferable to $EL_NHC$ when the perfectly conducting boundary condition is appropriate. For more complex conditions, $EL_NHC$ may be preferable.

**Acknowledgments.** I would like to thank Professor F. Santosa for several useful discussions regarding dispersion relations.

REFERENCES

[1] J. ADAM, A. SERVENIERE, J. NÉDÉLEC, AND P. RAVIART, *Study of an implicit scheme for integrating Maxwell's equations*, Comput. Methods Appl. Mech. Engrg., 22 (1980), pp. 327–346.

[2] F. BREZZI, *On the existence and uniqueness of saddle-point problems arising from Lagrange multipliers*, RAIRO Anal. Numér., 8-R2 (1974), pp. 129–151.

[3] A. CANGELLARIS, C.-C. LIN, AND K. MEI, *Point-matched time domain finite element methods for electromagnetic radiation and scattering*, IEEE Trans. Antennas and Propagation, AP-35 (1987), pp. 1160–1173.

[4] P. G. CIARLET, *The Finite Element Method for Elliptic Problems*, Vol. 4, Studies In Mathematics and Its Applications, Elsevier, North–Holland, New York, 1978.

[5] G. DUVAUT AND J.-L. LIONS, *Inequalities in Mechanics and Physics*, Springer–Verlag, New York, 1976.

[6] V. GIRAULT AND P. RAVIART, *Finite Element Methods for Navier–Stokes Equations*, Springer-Verlag, New York, 1986.

[7] G. GOLUB AND C. VAN LOAN, *Matrix Computations*, The Johns Hopkins University Press, Baltimore, MD, 1983.

[8] D. S. JONES, *The theory of electromagnetism*, MacMillan, New York, 1964.

[9] R. L. LEE AND N. K. MADSEN, *A mixed finite element formulation for Maxwell's equations in the time domain*, J. Comput. Phys., 88 (1990), pp. 284–304.

[10] R. LEIS, *Initial Boundary Value Problems in Mathematical Physics*, John Wiley, New York, 1988.

[11] P. MONK, *An analysis of Nédélec's method for the spatial discretization of Maxwell's equations*, SIAM J. Numer. Anal., 28 (1991), pp. 1610–1634.

[12] P. MONK, *A mixed method for approximating Maxwell's equations*, J. Comput. Appl. Math., to appear.
[13] J. NÉDÉLEC, *Mixed finite elements in* $\mathbb{R}^3$, Numer. Math., 35 (1980), pp. 315–341.
[14] P. A. RAVIART AND J. M. THOMAS, *A mixed finite element method for 2nd order elliptic problems*, in Mathematical Aspects of the Finite Element Method, A. Dold and B. Eckmann, eds., Lecture Notes in Math. 606, Springer-Verlag, Berlin, 1977.
[15] R. RICHTMEYER AND K. MORTON, *Difference methods for initial value problems*, Wiley-Interscience, New York, 1976.
[16] A. TAFLOVE, K. R. UMASHANKAR, B. BEKER, F. HARFOUSH, AND K. S. YEE, *Detailed FD-TD analysis of electromagnetic fields penetrating narrow slots and lapped joints in thick conducting screens*, IEEE Trans. Antennas and Propagation, 36 (1988), pp. 247–257.
[17] L. N. TREFETHEN, *Group velocity in finite difference schemes*, SIAM Rev., 24 (1982), pp. 113–136.
[18] K. YEE, *Numerical solution of initial boundary value problems involving Maxwell's equations in isotropic media*, IEEE Trans. Antennas and Propagation, AP–16 (1966), pp. 302–307.